Materials & Design 237 (2024) 112594

Contents lists available at ScienceDirect

Materials & Design

journal homepage: www.elsevier.com/locate/matdes

Multi-objective design of 3D phononic crystal waveguide by design space trimming

Sabiju Valiya Valappil, Johannes F.L. Goosen, Alejandro M. Aragón *

Faculty of Mechanical, Maritime and Materials Engineering, Delft University of Technology, Mekelweg 2, 2628 CD Delft, the Netherlands

ARTICLE INFO

Keywords:
Phononic crystal
Band structure
Transmissibility
Static analysis
Multi-objective design
Parametric sweeping
Sensitivity analysis

ABSTRACT

Ultrasonic flowmeters face unique challenges since, in addition to withstanding high fluid pressures, they have to avoid crosstalk, which is the interaction of the signals traveling through the fluid and the solid pipe. To avoid the crosstalk, which leads to poor accuracy or complete loss of the required signal, we develop a mounting mechanism based on phononic crystals (PnCs), which are artificial periodic materials possessing band gaps (BGs) due to Bragg scattering. These PnC structures should also possess high mechanical strength to sustain the fluid pressure. Designing PnCs for such applications is challenging as the BG width and the resistance to mechanical loading are conflicting objectives. To circumvent this, we propose a step-by-step design procedure to optimize both mechanical strength and wave attenuation performance of a single-phase 3D PnC waveguide using parametric sweeping and sensitivity analysis. We use finite element analysis (FEA) to characterize the behavior of the periodic unit cell and the waveguide. Since accurate dynamic FEA at high frequencies is computationally demanding, we develop surrogate models at different levels of the design process. We also consider additive manufacturing aspects in the design procedure, which we validate by 3D-printing the final design and measuring the parameters via computer tomography.

1. Introduction

Ultrasonic flowmeters are extensively used in industries such as oil and gas [1], aerospace [2], automotive [3], medical [4], and pharmaceutical [5], among others. One such instrument, an in-line transit-time flowmeter, measures the flow rate via ultrasonic transducers that are in contact with the fluid. An ultrasound signal generated by a piezoelectric element of the transmitter travels through the fluid and arrives at the receiver. This is repeated in the opposite direction, and the time difference between these signals is directly related to the flow rate. Since the flow is not disrupted during the measurement process, ultrasonic flowmeters possess high accuracy. Nevertheless, when the signal is sent, a significant part of it leaks through the solid pipe and interferes with the working signal from the fluid interface, known as crosstalk. Since crosstalk makes it hard to discriminate the required signal traveling through the fluid [6], several solutions have been proposed for crosstalk mitigation [7–10]. However, these approaches are limited by specific ranges of flow velocity, pipe diameter, and sound velocity of the medium [9]. Additionally, many of them operate at relatively low frequencies (approximately 100 kHz range [8]), which limits their applicability to high-frequency situations (for instance, at MHz frequencies).

Phononic crystals (PnCs) present a viable solution to mitigate crosstalk at high frequencies. PnCs are artificial materials consisting of periodically arranged unit cells possessing unusual dynamic characteristics due to band gaps (BGs) [11]. BGs are frequency ranges where elastic/acoustic waves are attenuated or propagate evanescently. These BGs are generated due to the destructive interference of waves because of the impedance mismatch at material interfaces within a periodic unit cell (PUC), similarly to Bragg scattering in electromagnetic waves [12]. Because of BGs, PnCs have been explored in many applications, including vibration isolation [13], acoustic diodes and transistors [14,15], energy harvesting [16], super/hyper acoustic lenses [17,18], acoustic antennas [19], frequency steering [20], acoustic cloaking [21–23], metasurfaces for phase manipulation [24,25], acoustic communication devices [26,27], and high-resolution acoustic devices [28].

BGs in PnCs are typically determined using a dispersion relation (band structure) [29], which is the relation between frequency and

* Corresponding author.
E-mail addresses: S.ValiyaValappil@tudelft.nl (S. Valiya Valappil), J.F.L.Goosen@tudelft.nl (J.F.L. Goosen), a.m.aragon@tudelft.nl (A.M. Aragón).
URLs: https://www.tudelft.nl/en/3me/about/departments/precision-and-microsystems-engineering-pme/people/junior-research-staff/valiya-valappil-sabiju/ (S. Valiya Valappil), https://3me.tudelft.nl/aaragon (A.M. Aragón).

https://doi.org/10.1016/j.matdes.2023.112594
Received 9 October 2023; Received in revised form 15 December 2023; Accepted 17 December 2023
Available online 27 December 2023

wave vector. The wave vector's magnitude is the wavelength's reciprocal, and its direction is towards the phase velocity [30]. The band structure provides the BG frequency range (if any) and the wave speeds. Nevertheless, since the band structure assumes infinite structure—i.e., a PUC repeated *ad infinitum*—it cannot capture the attenuation behavior of a finite system. A displacement transmissibility analysis is therefore necessary [31], which relates the amplitudes of the transmitted displacement (measured at one end of the waveguide) to the input displacement (at the opposite side where the essential boundary condition (BC) is prescribed), as a function of frequency. Systematic computational tools such as topology optimization have been used to design PnCs for maximizing BGs [32–41]. Topology optimization is an iterative procedure where forward analysis is used to analyze the design and sensitivity analysis is used to improve the design for the next iteration; this process continues until some measure of convergence is achieved. For instance, Sharma et al. used gradient-based topology optimization to maximize the BG width of electrostatically tunable dielectric PnCs [33]. A similar approach was used by Wu et al. to design PnCs with prescribed BG behavior [34]. Zhang et al. used topology optimization with a non-gradient-based algorithm to design a multi-channel narrow-band PnC filter [35]. A density-based topology optimization was used by Dalklint et al. to design PnCs with tunable BGs [36]. Zhang et al. designed a multi-functional metamaterial with tunable thermal expansion and BG through topology optimization and surrogate modeling [37]. van den Boom et al. used a level-set-based topology optimization to design 3D PnCs with smooth boundaries [38]. However, these approaches are computationally demanding since we may need several numbers of iterations to arrive at an optimized design. In addition, numerous issues are present while translating these designs to functional devices that can be used in ultrasonic flowmeters. The main challenge is with the fabrication as the feature size of the PnC's PUC can be in mesoscale (hundreds of microns to a few centimeters), which is difficult to manufacture [42]. Additionally, since the waveguide and the PUC (the waveguide is made of) have orders of magnitude differences in scale, requiring the manufacturing process to deal with both meso- and macro-scales, which is cumbursome. In addition, for the ultrasound flowmeter under a high fluid pressure situation, the device must possess a broad BG and high resistance against mechanical loading, further complicating the design process.

The primary objective of the PnC is to mitigate crosstalk, i.e., to filter out elastic waves traveling through the solid region for specific frequency ranges (in the MHz range). In our previous work, we developed a PnC wave filter to mitigate crosstalk from an ultrasonic flowmeter at high frequencies [43]. However, we did not optimize its performance, which requires several iterations of the complete waveguide's transmissibility analysis. This optimization is challenging since dynamic analyses of PnCs at high frequencies are computationally demanding while using standard computational approaches such as finite element analysis (FEA). This is because the PUC's complex geometry and the waveguide's large domain size (comprised of several PUCs) lead to a large number of degrees of freedom (DOFs). Moreover, the computational cost is further aggravated at high frequencies because a small finite element mesh size is required to maintain spatial and temporal accuracy [44]. Although optimization of PnCs' PUCs for BG maximization via band structure is feasible [38–41], it is nearly impossible to perform optimization of the complete model of a finite PnC structure using the transmissibility analysis due to the associated enormous computational cost. Thus, to efficiently optimize the performance of the PnC waveguide at high frequencies, a surrogate model—i.e., an approximate model that is computationally less expensive than the complete model but which captures its behavior with sufficient accuracy—is required. For instance, Yin et al. applied dynamic condensation for band structure and transmission analysis of PnCs, where they reduced the computational cost by condensing internal DOFs to the boundary [45]. Similarly, Aumann et al. reduced the computational cost of the dynamic analysis of acoustic metamaterials by using a parametric model order reduction approach based on Krylov's subspaces' moment-matching methods [46]. However, no surrogate models have been developed to analyze 3D PnCs with applications in ultrasonic flowmeters. In addition to the aforementioned challenges associated with computational demands, the PnC design process is further complicated by environmental conditions such as the surrounding fluid pressure, which impose additional requirements and constraints.

One such requirement for the PnC structure is to have a fully closed construction. This is important because transducers, where these waveguides are connected, are immersed in fluid; thus, any fluid leakage into these structures could reduce their performance. Additionally, the pressure from the surrounding fluid (approximately 15 MPa) also imposes an immense mechanical load on the PnC waveguide, and thus an additional objective for the design process. Designing a PnC waveguide with a broad BG and appropriate mechanical strength is challenging since they are both conflicting objectives. High contrast in mass densities and/or stiffnesses between adjacent constituents of the PUC is needed for a wide BG [47], which creates weak members within the PUC. The high-pressure load surrounding the PnC waveguide induces tremendous stress in these thin members, which are likely to undergo yielding. The effects of hydrostatic loading on 1D PnCs were explored by Mehaney and Elsayed [48], who found a shift in BG frequency with increased pressure. However, works that study the effect of hydrostatic pressure on 3D complex PnC structures are still lacking. To the best of our knowledge, no studies have addressed the multi-objective design of PnCs for maximizing the BG width and mechanical strength, incorporating additional aspects such as manufacturing processes and industrial standards.

In this study, we introduce for the first time a 3D PnC waveguide capable of mitigating high-frequency broad-band acoustic noise at MHz ranges under high hydrostatic pressure. To that end, we propose a design procedure to maximize the wave attenuation and minimize the stresses due to high fluid pressure. We also consider manufacturability, domain-size considerations, and industrial standards in the design process. We divide the problem into independent and dependent subproblems. Independent problems, such as the design of the PUC and the waveguide, are performed separately, while dependent portions, such as different analyses of the waveguide, are solved simultaneously. We also develop a surrogate model to reduce the computational cost of the waveguide's static and dynamic analyses. Since this is a multi-objective design problem, there will be a Pareto set of optimal designs, and our objective is to move towards such a front with our designs. To that end, we use the parametric sweep to move towards optimum designs by design space trimming. Further, we use sensitivity analysis to arrive at an optimized design that satisfies all constraints, which is fabricated via metal additive manufacturing. We then evaluate the quality of the fabrication process by measuring the different parameters of the PnC waveguide using computer tomography. The various steps in the proposed methodology can be applied as a whole or in parts to other multi-objective challenging design problems (e.g., periodic structures with time-consuming conflicting objectives) with appropriate modifications in the design steps.

2. Problem statement

Fig. 1 shows the schematic representation of an in-line ultrasonic flowmeter where the working signal traveling through the fluid is marked using green arrows while the signal traveling via the solid region is represented using a dotted red arrow. Since we want to avoid their crosstalk, a PnC waveguide is placed between the piezoelectric crystal and the adjacent pipe wall as shown in Fig. 1(b). The surrounding fluid exerts a high pressure p on the transducer and the associated PnC waveguide.

1. The ultrasonic transducer uses a pulse with a central frequency of 1 MHz, which should be the input signal for the PnC waveguide,

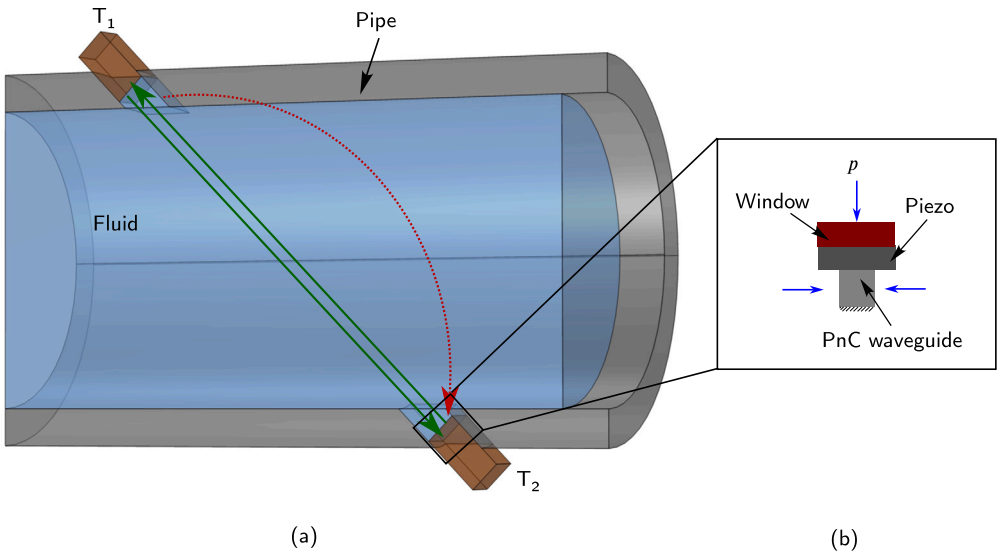

Fig. 1. Schematics of in-line ultrasonic flowmeter: (a) is a fluid-filled pipe with two ultrasound transducers T_1 and T_2 where the working signal (green arrows) and the signal via the solid region (dotted red arrow) are provided. The inset in (b) shows the portion of the ultrasonic transducer with a window (to transmit the acoustic energy to the fluid) and a PnC waveguide loaded by a hydrostatic pressure load of magnitude p.

and hence, the waveguide should possess a BG with its central frequency close to 1 MHz, and a width at least 600 kHz;

2. Fluid seepage into the waveguide should be prevented, causing a reduction in impedance contrast within the PnC, which leads to a reduction in performance. Thus, the PnC device should be closed entirely from the outside;
3. As the flowmeter is exposed to a high-pressure environment, the waveguide should be able to withstand a pressure load of up to 15 MPa. Because the high pressure could be detrimental to the internal features of the PUC, the enclosure should have the additional function of withstanding the high-pressure load;
4. The device should be designed to operate in a wide range of temperatures, from −150 °C till 600 °C, and the material should have a melting point beyond 600 °C;
5. The waveguide should be able to fit within the flowmeter (cylindrical shape), for which the lateral dimension of the PnC waveguide should be less than 18 mm;
6. Finally, the PnC device should be manufacturable with considerable accuracy and precision (repeatability) at a reasonable cost.

We then derive the following objectives:

Objective 1: Maximize the PnC waveguide's wave attenuation performance in the frequency range from 700 kHz to 1.3 MHz with the highest attenuation close to 1 MHz;

Objective 2: Minimize stress throughout the PnC structure when subjected to the pressure load of 15 MPa. Thus, the maximum stress developed in the structure should be less than the allowable stress, $\sigma_A = \sigma_Y/\gamma$, where σ_A is the allowable stress, σ_Y is the yield strength, and γ is the safety factor of the material.

To satisfy some of the design requirements in order to reduce the design space, we take the following design decisions:

- We select stainless steel 316 (SS316) as the preferred material for the PnC waveguide since it has low thermal expansion (17.2×10^{-6}/°C) and a high melting point (1375 °C) to address the thermal requirements. Additionally, since the transducer and associated structures are usually composed of SS316, using the same material for the PnC structure would minimize the thermal stress generation at interfaces;
- We consider a hexagonal PUC for the 3D PnC since it can be arranged close to a cylindrical shape to satisfy the 5th design requirement above, i.e., to have a diameter less than 18 mm;
- Since the waveguide needs to be connected to the ultrasonic transducer, two hollow-cylindrical fixtures are included in the design, which would ensure adequate contact between the transducer and the waveguides;
- As BGs in PnCs are generated via Bragg scattering, we can estimate the outer dimension of the PUC from Bragg's law of diffraction by using the sound speed in the material and the required central frequency as follows:

$$n\bar{\lambda} = 2d\cos\theta \qquad \bar{\lambda} = c/f, \tag{1}$$

where n is an integer generally considered to be unity, $\bar{\lambda}$ is the wavelength of the traveling wave in the material, θ is the angle the wave creates with the normal of the incidence surface, d is the periodicity of the scatterer (in the case of a PnC, it is equivalent to the distance between the PUCs), c is the wave speed of the material, and f is the applied frequency. For SS316, the wave speeds are $c_P = 4935.5$ m/s for pressure wave and $c_S = 3102.9$ m/s for shear wave. For a normal incident wave, at 1 MHz, d is approximately 2 mm, which is selected as the outer dimension of the PUC;
- The PUC's length scale greatly influences the PnC waveguide's manufacturing process. Since the outer dimension of the PUC is 2 mm with a possibility to have even smaller (sub-millimeter) internal features, the available fabrication methods for SS316 are additive manufacturing [49] and wire electric discharge machining [50]. Since, at a prototype stage, the latter is more expensive than the former (two orders of magnitude), we select additive manufacturing as the preferred manufacturing process.

3. Design process

To design a PnC waveguide that can satisfy the design requirements, we describe the design process through various steps, as shown in Fig. 2.

Step-1: We define various building blocks that will be used throughout the process;

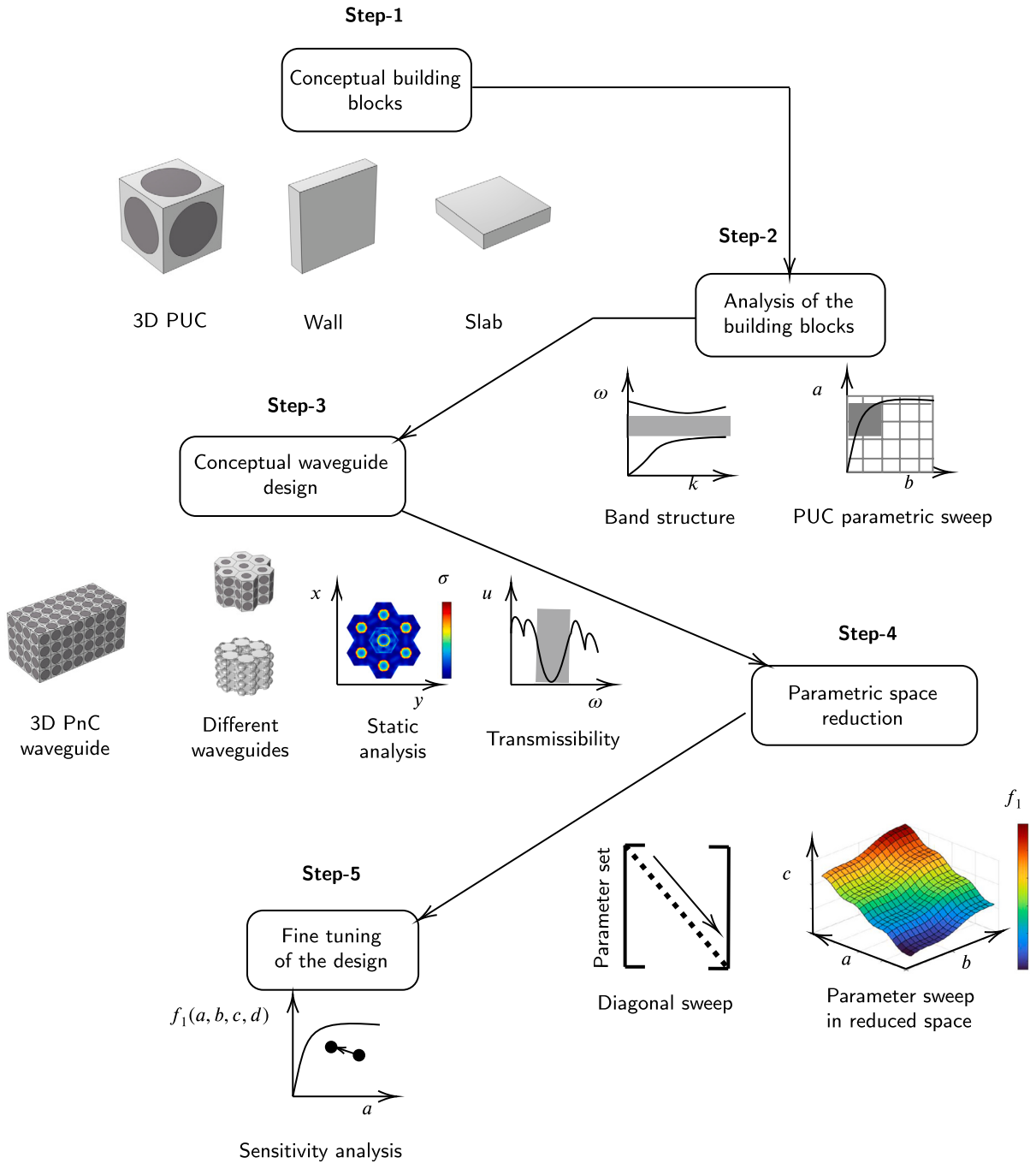

Fig. 2. Schematic of the design process with individual steps providing a global picture. Step-1 includes all the building blocks that constitute the design, whereas Step-2 describes the analysis of the building blocks. Step-3 consists of different waveguide designs and their analyses, while Step 4 encompasses the parametric space, the design space reduction method, and the parametric sweep to obtain nominal designs. Finally, Step-5 explains the fine-tuning process to attain optimal designs for the required problem.

Step-2: To design the PUCs, we perform different analyses of the building blocks;

Step-3: Using the build blocks, we design the complete waveguide, which is also characterized using several analyses;

Step-4: To find an optimized design satisfying the objectives, we conduct design space survey for adequate designs, followed by parametric sweeping;

Step-5: In the final step, we fine-tune the design using sensitivity analysis.

3.1. Step-1 – Conceptual building blocks

We need appropriate 3D PnC PUC that would provide adequate BG frequency range as required by **Objective 1**. Additionally, we also select an outer wall to enclose the waveguide and a slab to increase the strength in order to satisfy the design requirements (**Objective 2**). **Step-1** of the Fig. 2 shows the schematics of all these building blocks (3D PUC, wall, and slab). Since these schematics do not show the exact building blocks, we proceed to Fig. 3 for a detailed description; however, we will come back to Fig. 2 when discussing the different design

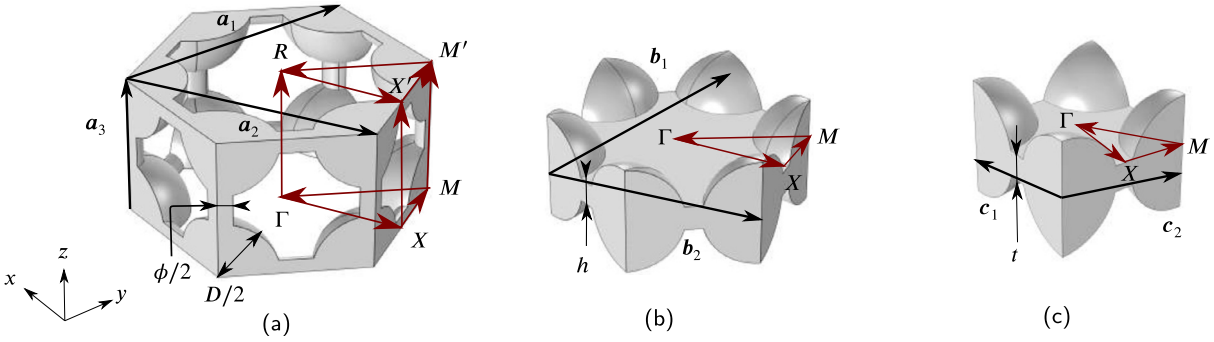

Fig. 3. Schematics of different PnC's PUC and their corresponding irreducible Brillouin zones. (a) a 3D hexagonal PUC, where $\boldsymbol{a}_i$ (i = 1 to 3) defines its lattice vector. We have translated $\boldsymbol{a}_1$ and $\boldsymbol{a}_2$ along the z-axis for visibility; however, this operation does not change the magnitude of these parameters. (b) and (c), respectively, are the 2.5D hexagonal and square PUCs with corresponding lattice vectors, i.e., $\boldsymbol{b}_i$ (i = 1 to 2) for hexagonal and $\boldsymbol{c}_i$ (i = 1 to 2) for square PUCs. (d) the IBZ of the 3D hexagonal PUC (triangular prism), while (e) and (f), respectively, the IBZs of 2.5D hexagonal and square PUCs (both are triangles). Additionally, we have marked the design parameters: rib diameter ϕ and sphere diameter D in (a), slab thickness h in (b), and wall thickness t in (c), respectively.

stages. Previously, van den Boom et al. used topology optimization to maximize the BG of a 3D PUC, showing that a spherical cavity maximized the width of the band gap [38]. Since the primary objective of our PnC-based waveguide is to have a broad BG, we design a hexagonal PUC possessing spherical features as shown in Fig. 3(a). This PUC is designed by connecting spheres with cylindrical rods since this combination provides a wide BG [43] and is a single-phase component. In other words, the BG is generated because of the mismatch in the mass and stiffness between the adjacent sphere and the rod, i.e., dissimilarity in the mechanical impedance, unlike due to the acoustic impedance mismatch in multi-phase PnCs. A similar PUC composed of spheres and ribs with the cubic arrangement was used in our previous work, which also possessed a broad BG [43]. We also performed experiments on this earlier prototype (fabricated via metal additive manufacturing) to characterize the 3D PnC waveguide's performance at MHz frequency ranges, and thus validated the BG predicted numerically. There the spheres were in the middle of the ribs, resulting in challenges during fabrication using additive manufacturing due to the large overhang angles. We address that problem in this work by positioning the spheres at the intersections of the ribs, thereby reducing the overhang angles (see Fig. 3(a)). We define two design parameters for the PUC: the sphere diameter D and the rib diameter ϕ, which are later used in a parametric sweep to obtain the widest BG frequency range. Fig. 3(a) also shows the lattice vectors $\boldsymbol{a}_1$, $\boldsymbol{a}_2$, and $\boldsymbol{a}_3$, although for visualization $\boldsymbol{a}_2$ and $\boldsymbol{a}_3$ have been translated to the top of the PUC. Fig. 3(b) and 3(c), respectively, represent the 2.5D hexagonal and square PUCs that are used to design the outer wall and the internal slabs. These structures are called 2.5D PnCs because they lack the periodicity in the third direction (z-direction), although they are 3D structures. We have also marked lattice vectors in the corresponding PUCs ($\boldsymbol{b}_1$ and $\boldsymbol{b}_2$ in Fig. 3(b) and $\boldsymbol{c}_1$ and $\boldsymbol{c}_2$ in Fig. 3(c), respectively). Since 2.5D PUCs are also made of the same material (SS316) as that of the 3D PUC, their lattice parameters' magnitudes are also the same for the 1 MHz BG central frequency. Thus $\|\boldsymbol{b}_1\| = \|\boldsymbol{a}_1\|$, $\|\boldsymbol{b}_2\| = \|\boldsymbol{a}_2\|$, and $\|\boldsymbol{c}_1\| = \|\boldsymbol{c}_2\| = \|\boldsymbol{a}_3\|$. Two additional design parameters, the slab thickness h and the wall thickness t, are defined and later used in the parametric sweeping of the complete waveguide design in **Step-4**.

To obtain the BG behavior of the aforementioned PUCs, we need to perform the dispersion analysis as mentioned in the introduction. To that end, we transform the PUCs from the Bravais lattice to the reciprocal lattice, where they are represented using Brillouin zones (BZs) [51]. The smallest section of the Brillouin zone that can accurately capture the band structure of the PUC is called the irreducible Brillouin zone (IBZ) [51]; the more symmetries the PUC possesses, the smaller the IBZ. Since the 3D hexagonal PUC has 24-fold symmetry, the resulting IBZ is a triangular prism (marked using maroon arrows in Fig. 3(a)). Similarly, the 2.5D hexagonal and square PUCs, respectively, possess 12- and 8-fold symmetries; thus, they have triangular IBZs, which are also marked using maroon arrows in Fig. 3(b) and 3(c). To design these PUCs for broad BGs centered around 1 MHz, we carry out their analysis using the band structure analysis as described next.

3.2. Step-2 – Analysis of the building blocks

Since both the 3D and 2.5D PnC structures are solely composed of solid material, the wave propagation is governed by the elastic wave equation:

$$\rho\ddot{\boldsymbol{u}} = (\lambda + 2\mu)\Delta\boldsymbol{u} - \mu\nabla\times\nabla\times\boldsymbol{u}, \tag{2}$$

where $\boldsymbol{u}(\boldsymbol{x},t)$ and $\ddot{\boldsymbol{u}}(\boldsymbol{x},t)$, respectively, are the spatial displacement and acceleration as functions of position $\boldsymbol{x}$ and time t. ρ is the density of the material, and λ and μ are the Lamé coefficients; Δ and $\nabla\times$ are, respectively, the 3D Laplacian and curl operators. To fully define the boundary value problem, Equation (2) needs to be supplemented by appropriate boundary conditions (BCs).

3.2.1. Band structure analysis

The band structure analysis is performed by applying Bloch-Floquet periodic boundary conditions [52] along the boundaries of the PUC where the wave vector values are restricted to the IBZ, as follows:

$$\boldsymbol{u}(\boldsymbol{x}+\boldsymbol{a}_i,t) = e^{i\boldsymbol{k}\cdot\boldsymbol{a}_i}\boldsymbol{u}(\boldsymbol{x},t), \tag{3}$$

where $\boldsymbol{k} = \left(k_x, k_y, k_z\right)$ is the 3D wave vector [53] and $\boldsymbol{a}_i, i = \{1\ldots3\}$ are lattice vectors as shown in Fig. 3(a). By using FEA via the $\omega(\boldsymbol{k})$ approach – calculating frequencies for given values of wave vectors [54], we obtain the band structure of both 3D and 2.5D PUCs. Fig. 4a represents the band structure of 3D hexagonal PUC obtained for the design parameters $\phi = 0.4$ mm and $D = 1.6$ mm (not the optimal case with respect to the BG width), with the shaded region showing the BG, while the BZ and IBZ are shown in the inset. We calculate 40 wavebands through 8 branches of the IBZ, with a total of 96 wave vector steps (12 steps per branch) to obtain the dispersion relation up to 2 MHz. We observe a BG between the 11^{th} and 12^{th} wavebands that spans for 815.6 kHz ($f_{H2} - f_{H1}$). Note that this PUC design satisfies the BG requirement; however, the remaining requirements still need to be satisfied.

We also investigate the dispersion relation of the 2.5D square (Fig. 3(b)) and hexagonal (Fig. 3(c)) PUCs by the same approach. Here we use corresponding lattice vectors ($\boldsymbol{c}_i$ for square and $\boldsymbol{b}_i$ for hexagonal) and IBZs (Fig. 3(c) for square and 3(b) for hexagonal, respectively). Figs. 4b and 4c represent band structures of square and hexagonal lattices, respectively, where shaded regions represent corresponding BGs. In the case of the square lattice, we calculate 30 wavebands through 3 branches of the IBZ with 36 wave vector steps in total (12 steps per

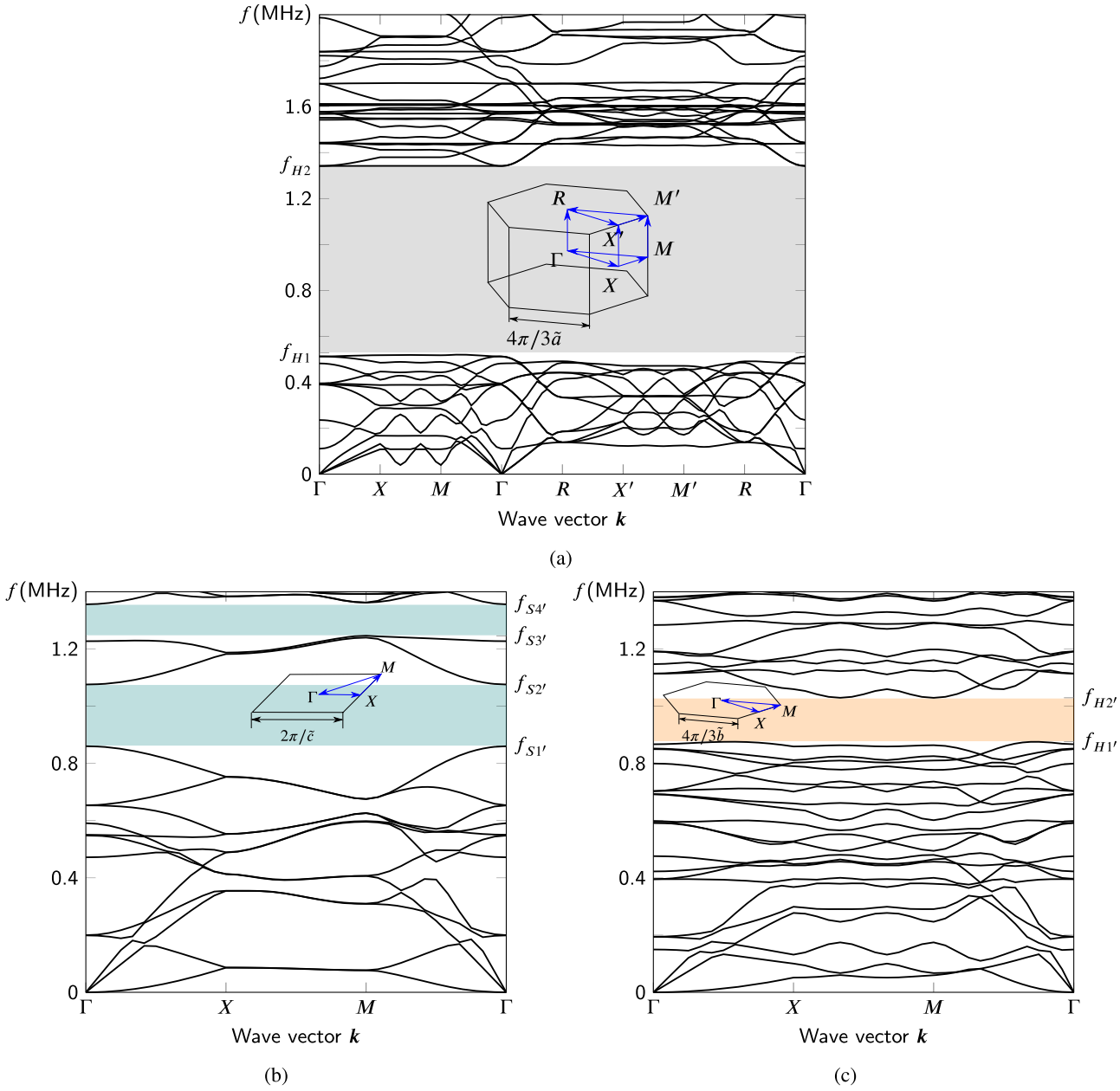

Fig. 4. (a) Band structure of the 3D PUC hexagonal lattice of Fig. 3(a) calculated up to 2 MHz, where the shaded region represents the BG. $f_{H1} = 0.53$ MHz and $f_{H2} = 1.34$ MHz define the extent of the hexagonal PUC's BG frequency range. The inset shows the hexagonal BZ with its IBZ (triangular prism), where $\tilde{a} = \|\boldsymbol{a}_3\| = 2$ mm. Similarly, (b) and (c) are, respectively, the band structures of 2.5D PnCs with square and hexagonal PUCs, where the shaded regions represent corresponding BGs. The BG near 1 MHz in the square PUC is bounded by $f_{S1'} = 0.86$ MHz and $f_{S2'} = 1.08$ MHz, while $f_{H1'} = 0.87$ MHz and $f_{H2'} = 1.03$ MHz are the bounding frequencies of the hexagonal PUC. Additionally, as shown in (b), the second BG in the square PUC is between $f_{S3'} = 1.24$ MHz and $f_{S4'} = 1.36$ MHz. The insets in (b) and (c), respectively, show the square BZ with its IBZ (triangular) and the hexagonal BZ with its IBZ (also triangular), where $\tilde{c} = \tilde{b} = 2$ mm.

branch) to get the dispersion relation till 1.6 MHz. For the square PUC, two BGs are present, out of which, the first one is between 12$^{\text{th}}$ and 13$^{\text{th}}$ branches, and spans for 215.8 kHz ($f'_{S2} - f'_{S1}$). The second BG is present between 14$^{\text{th}}$ and 15$^{\text{th}}$ branches, and has a frequency range of 153 kHz ($f'_{S4} - f'_{S3}$). In the case of the hexagonal lattice, 50 wavebands are calculated through 3 branches of the IBZ with the same number of wave vector steps as in the square lattice to obtain the band structure up to the same frequency (1.6 MHz). We can see a BG between the 21$^{\text{st}}$ and 22$^{\text{nd}}$ branches, which is 154 kHz wide. Notably, although the 2.5D PUCs' BGs are considerably narrower than that of the 3D PUC, the formers' primary functions are to prevent fluid leakage and provide structural strength to the waveguide. Thus, a narrow BG close to 1 MHz would be sufficient for the 2.5D PUCs since the frequencies containing the largest energy contributions are close to 1 MHz. Moreover, since the waveguides have to mostly deal with bulk waves rather than surface waves, the influence of 2.5D PnCs on the wave attenuation would be low. We now perform a parametric sweep to obtain optimum ranges for the design parameters ϕ and D and remove part of the design space that does not produce any BG.

3.2.2. 3D PUC's parametric sweep

We identified the relevant design parameters from the building blocks as the sphere diameter D, the rib diameter ϕ, the wall thickness t, and the slab thickness h. The lower bound of these parameters is provided by the resolution of the manufacturing process, for which additive manufacturing was selected in the decision phase. Their up-

Table 1
Global ranges of design parameters subjected to manufacturing constraints and domain limitations. All parameters are represented in terms of a dimensionless parameter ξ, so we can vary them simultaneously during the diagonal sweeping.

Parameters	Min. (mm)	Max. (mm)	range in ξ (0 to 1)
Rib diameter ϕ	0.2	1.5	$0.2 + 1.3 \times \xi$
Sphere diameter D	0.2	2	$2 - 1.8 \times \xi$
Wall thickness t	0.2	1.5	$0.2 + 1.3 \times \xi$
Slab thickness h	0.2	1.5	$0.2 + 1.3 \times \xi$

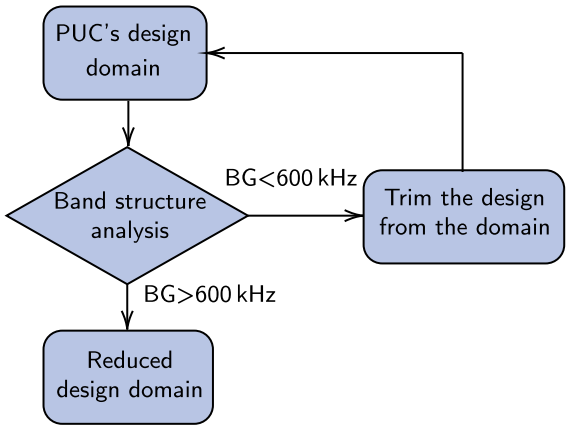

Fig. 5. The flowchart showing the PUC's parametric sweep, where band structure analysis is performed while stepping through the PUC's design domain (ϕ and D). The designs with narrow BG width (BG < 600 kHz) are removed from the domain.

per bound is limited by the outer dimension of the PUC (see Table 1). Here we perform a parametric sweep over D and ϕ in order to identify the parameter combinations that produce a desirable BG width greater than 600 kHz, and in the process, we trim the remaining design space of ϕ and D as shown in Fig. 5. To that end, we step through the design space with a step size of 0.05 mm and calculate the BG width in every configuration of parameters. Since we need to conduct several band structure analyses, we have to minimize the computational cost per analysis. Thus, we limit the calculations to the 12^{th} waveband and restrict the eigenvalue analysis to four points per IBZ branch (a total of 32 points instead of 96). These modifications result in a tremendous decrease in the computational cost, from 50 min to 45 s per band structure.

Fig. 6 shows the results of this parametric study. The figure shows the BG width as a function of the design parameters ϕ and D. Noteworthy, regions of the design space that do not produce any BG are trimmed from the design space and excluded from this plot. Additionally, the dimensions that are too close to the lower bound are also eliminated because of difficulty in manufacturing. Thus the parameter ranges shown in Fig. 6 are: ϕ from 0.3 mm to 1 mm and D from 1 mm to 2 mm. The figure shows that the BG width increases with a decrease in ϕ and an increase in D as this combination increases the variation in the mass and stiffness and, thus, the mechanical impedance contrast between the rib and the sphere. However, the BG starts to decrease after $D = 1.6$ mm (see Fig. 6) as a further increase in D results in a decrease in the stiffness contrast. This is because the adjacent spheres become very close, resulting in short connecting ribs, thus increasing the rib stiffness and eventually reducing the BG width. Fig. 6 also provides information about the parameter combinations that produce narrow BGs (< 600 kHz), which are excluded hereafter from further analysis (refer to the non-shaded regions from Fig. 6). Thus we select ranges of ϕ from 0.3 mm to 0.54 mm and D from 1.42 mm to 1.875 mm (refer to the hatched region in Fig. 6). After trimming the PUC's design space, we move towards PnC waveguide design.

3.3. Step-3 – Conceptual waveguide design

3D PnC waveguides are formed by stacking the PUCs in all three directions as shown in the schematic of **Step-3** in Fig. 2. To create the waveguide design, we arrange seven 3D hexagonal PUCs in one layer ($x - y$ plane), which is then stacked (ten layers) in the out-of-plane (z) direction as shown in Fig. 7(c). The enclosure is then added by using the 2.5D square (Fig. 7(b)) and hexagonal (Fig. 7(a)) waveguides covering the entire outer surface. Furthermore, as described in Fig. 7(c), two cylindrical fixtures of diameter 4 mm, height 4 mm, and wall thickness 0.5 mm are added at both ends (perpendicular to the $x - y$ plane) to connect to the transducers. This waveguide's wave propagation performance and the resistance against mechanical loading are characterized by means of transmissibility and static analysis, respectively.

3.3.1. Transmissibility analysis of the PnC waveguide with enclosure

The transmissibility analysis provides us with the attenuation rate of the supplied elastic wave for a certain number of spatially arranged PUCs at a particular frequency. This analysis can be used to design the total number of PUCs and their orientation in space corresponding to a required attenuation rate. Thus, transmissibility analysis adds an additional design parameter, the number of layers n, to the parameters from Table 1, which we can use to tune the wave attenuation performance of the waveguide.

The displacement transmissibility analysis is carried out by prescribing essential (Dirichlet) BCs [55] $\bar{\boldsymbol{u}}$ at one end of the waveguide as shown in the hatched pattern in Fig. 7(c). The Dirichlet BC takes the form:

$$\boldsymbol{u}(\boldsymbol{l}, t) = \bar{\boldsymbol{u}} e^{i\omega t}, \tag{4}$$

where $\bar{\boldsymbol{u}}$ is the constant displacement imposed at one end (left end), ω is the applied frequency in rad/s, and $\boldsymbol{l}$ represents position vectors of the ring-shaped hatched surface of the waveguide's left fixture (marked in Fig. 7(c)). For this analysis, the remaining boundaries of the waveguide are free from traction. As the transmissibility analysis is computationally expensive due to the large number of DOFs and many frequency steps, we need to reduce its computational cost to perform several transmissibility analyses. To that end, we generate a minimalistic model that can capture the dynamic response of the complete PnC waveguide while minimizing the computational cost. Thus, we perform the transmissibility analysis on PnC waveguides with different numbers of layers while preserving their cross-sectional topologies. Since a one-layer waveguide does not provide the attenuation rate due to the lack of interfaces (between layers) to generate the BG, we investigate the transmissibility of waveguides with 2, 4, 6, 8, and 10 layers. All these designs look similar to the design from Fig. 7(c) with varying heights (towards z-direction). This approach allows us to compare their dynamic responses since the geometric variation only occurs in one direction, and thus, the attenuation rate varies with a single spatial coordinate (z).

To compare the BG width between the band structure and transmissibility analysis, we select the same values for the design parameters from the band structure study, i.e., $\phi = 0.4$ mm and $D = 1.6$ mm. Additionally, here we select the wall thickness, $t = 0.4$ mm to be consistent with the rib diameter, which would reduce complexities during finite element meshing. The analyses are performed by providing a continuous harmonic displacement of 1 μm amplitude for a frequency range from 0.3 MHz to 1.5 MHz with a step of 10 kHz. The resulting transmissibility relations for waveguides with different number of layers (2, 4, 6, 8, and 10) are plotted in Fig. 8, where the BGs predicted by band structure analyses of 3D PUC is shown using gray shaded region, while the blue shaded and orange hatched regions are, respectively, BGs of 2.5D cubic and hex PUCs. The geometry, along with the Dirichlet BC of the 2-layer PnC waveguide, is also shown in the inset of Fig. 8. As shown

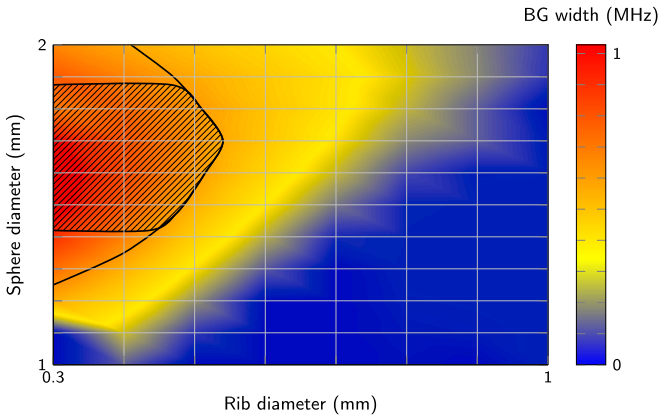

Fig. 6. Surface plot showing the BG width (in MHz) as a function of rib and sphere diameters, where the isoline represents a BG width of 600 kHz. The rib diameter, ϕ varies from 0.3 mm till 1 mm, whereas the sphere diameter, D varies from 1 mm to 2 mm. Although the BG width increases with an increase in D and a decrease in ϕ, it starts to reduce beyond $D \approx 1.6$ mm. This is because large spheres reduce the length of the interconnecting ribs, resulting in increased rib stiffness and, consequently, decreased stiffness contrast between spheres and ribs. The hatched region (ϕ from 0.3 mm to 0.54 mm and D from 1.42 mm to 1.875 mm) in the plot shows parameter ranges corresponding to the acceptable BG width.

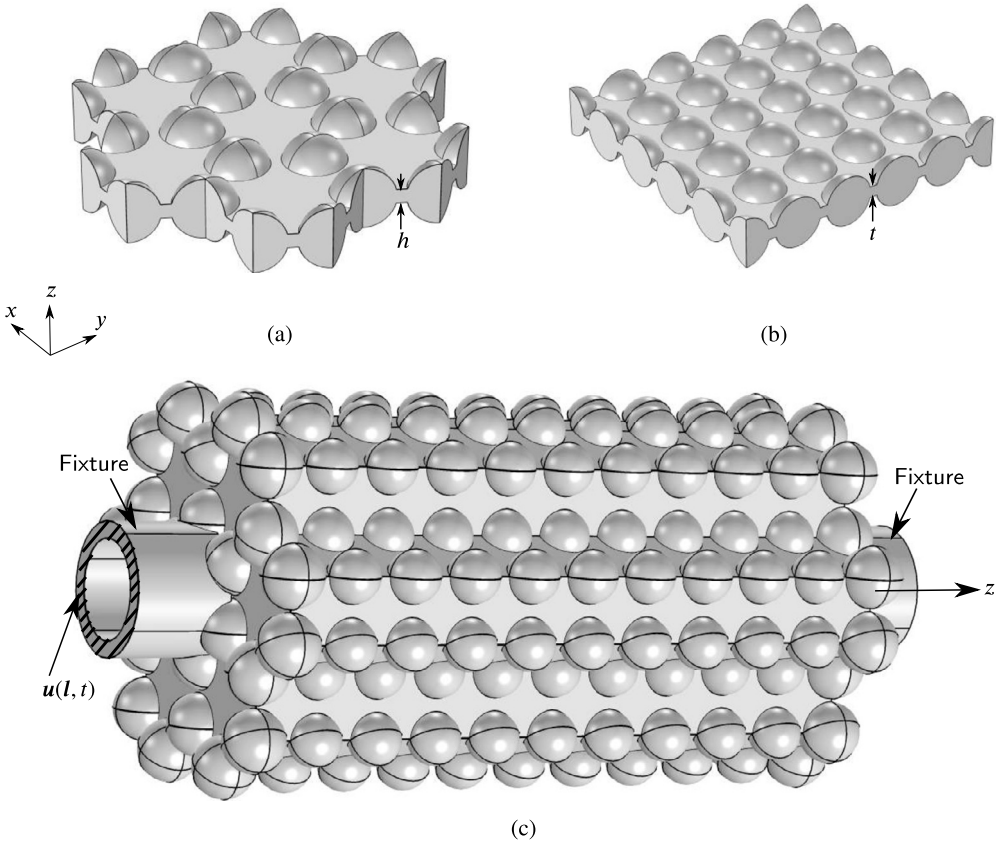

Fig. 7. Geometries of 2.5D PnCs' waveguides and the enclosed PnC waveguide. (a) and (b) are 2.5D hexagonal and cubic PnC waveguides. (c) the complete PnC waveguide consisting of 3D hexagonal PUCs as internal structures, while 2.5D cubic PUCs are used to close the side walls. Moreover, 2.5D hexagonal PUCs are applied to the top and bottom faces to close the PnC structure entirely. (c) also contains two fixtures (marked using arrows) for connecting the waveguide to the rest of the transducer. The Dirichlet BC is also provided in (c) on the hatched region.

in the figure, the waveguide with ten layers captures the attenuation response (BG) predicted by the band structure analysis of the 3D PUC, with the highest attenuation rate at 1.04 MHz. We can also observe that the highest attenuation region is where the BG from the 3D PUC overlaps with 2.5D PUCs because, in the remaining frequency ranges, the enclosure does not possess a BG, which reduces the attenuation rate. Additionally, several peaks are present within the BG due to reflections from the free surfaces (outer surfaces of the enclosure), which the band structure analysis cannot capture. However, in actual applications, the PnC waveguides are connected to the transducer (via the fixtures), and part of the energy is transmitted through these interfaces, reducing the reflection peaks. Additionally, these peaks are further reduced by the influence of the surrounding fluid, which channels the wave energy through the waveguide-fluid interface. Moreover, the targeted application involves a pulse instead of a continuous signal (as mentioned in the problem statement), further reducing the reflections. Since accommo-

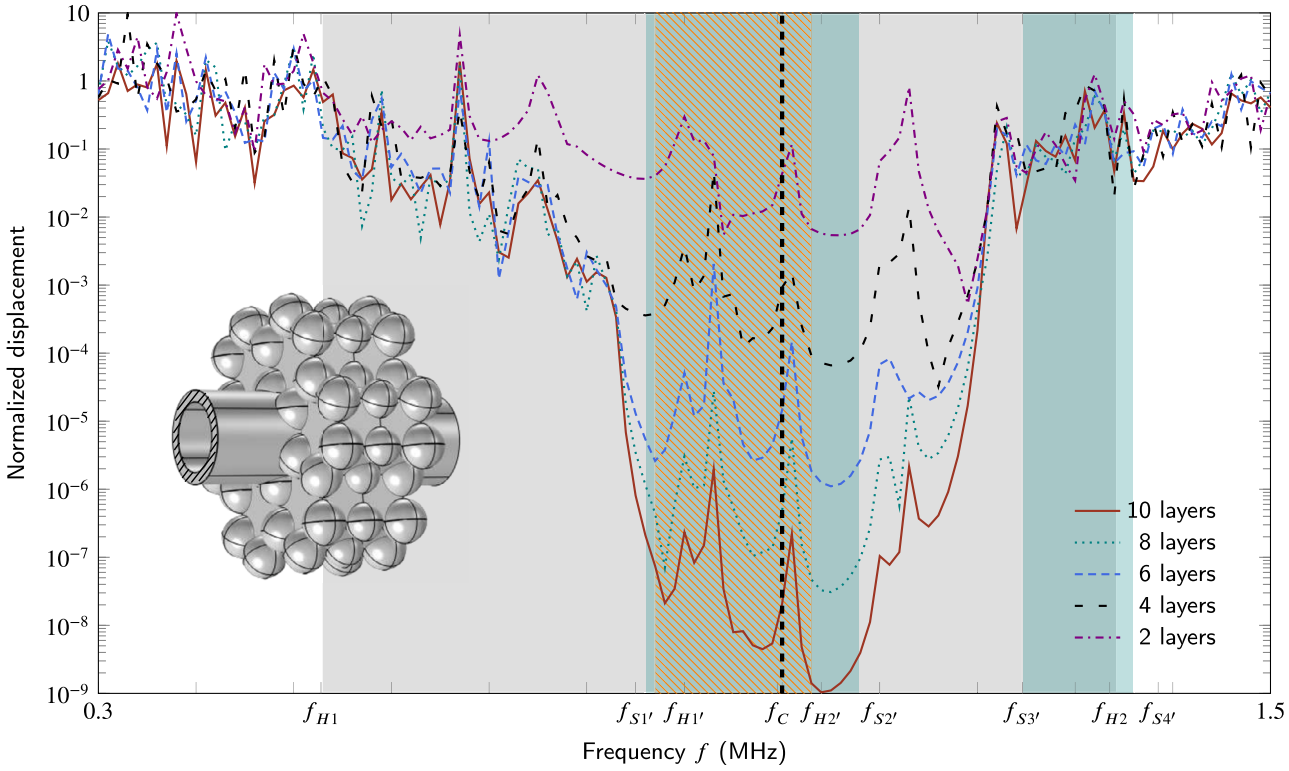

Fig. 8. Transmissibility responses of hexagonal PnC waveguides with the different number of layers calculated from 0.3 MHz to 1.5 MHz with a frequency step of 10 kHz. The shaded (and hatched) regions represent BGs predicted by the 3D hexagonal (f_{H1} to f_{H2}), 2.5D square ($f_{S1'}$ to $f_{S2'}$ and $f_{S3'}$ to $f_{S4'}$), and 2.5D hexagonal ($f_{H1'}$ to $f_{H2'}$) PUCs with parameters $\phi = 0.4$ mm, $D = 1.6$ mm, and $t = 0.4$ mm. A 2-layer PnC waveguide with the Dirichlet BC is shown in the inset. The accuracy in capturing the dynamic response of the complete waveguide (10 layers) decreases with a decrease in the number of layers; thus, the model with six layers is selected since it captures most of the dynamic behavior of the complete model.

dating all these conditions is practically impossible during parametric sweeping in the later stage, we then apply low-reflection BCs around the waveguide (all outer surfaces except for the hatched region from Fig. 7(c)).

In addition to checking the attenuation response of the PnC waveguide, as discussed before, the transmissibility study in this section is used to determine a minimalistic model of the complete waveguide. As evident from Fig. 8, designs with two and four layers fail to capture the actual trend of the waveguide's dynamic behavior of the complete model. In other words, they could not represent the changes in attenuation rate with respect to frequency and the peaks of the 10-layer PnC waveguide. The six-layer model, however, shows the dynamic response of the entire model more accurately with a nominal computational cost, so it is selected for further transmissibility analyses. After selecting this model and obtaining the transmissibility response, we proceed with the static stress analysis of the PnC waveguide.

3.3.2. Static stress analysis

To check the performance of the enclosed PnC waveguide against a fluid pressure load (as required in **Objective 2**), we conduct static analysis. This analysis is carried out after fixing the hatched region, where previously a harmonic displacement was prescribed for the transmissibility analysis (refer Fig. 7(c)) and by applying a uniform pressure load of 15 MPa on all its remaining outer surfaces, since the entire waveguide is immersed in the fluid. The required BCs can be written as a combination of Dirichlet and Neumann BCs as follows:

$$\boldsymbol{u}(\boldsymbol{l}) = \boldsymbol{0}; \tag{5}$$

and,

$$\boldsymbol{\sigma} \cdot \boldsymbol{n} = \bar{\boldsymbol{t}} = -p\boldsymbol{n}, \tag{6}$$

where $\boldsymbol{\sigma}$ represents Cauchy's stress tensor, and $\boldsymbol{n}$ is the outward normal evaluated on the entire waveguide boundary. $\bar{\boldsymbol{t}}$ is the traction generated due to the applied pressure load p. We use von Mises stress throughout the structure as a measure of stress [56] since it correlates with the yield criteria of ductile materials such as SS316. The maximum stress obtained by the static analysis, $\sigma_{\max}$ is compared against the allowable stress of the material to evaluate the mechanical performance as described in **Objective 2**:

$$\sigma_A = \frac{\sigma_Y}{\gamma} = \frac{400\,\text{MPa}}{2} = 200\,\text{MPa}, \tag{7}$$

where σ_Y is the yield stress for a SS316 structure fabricated via additive manufacturing [57] and $\gamma = 2$ is the safety factor selected from international standard ISO 2531 [58].

Figs. 9(a) and 9(b), respectively, show the cross-sectional (CS) and longitudinal sectional (LS) views of von Mises stress distribution of the 10-layer PnC waveguide with the same design parameters as the transmissibility analysis ($\phi = 0.4$ mm, $D = 1.6$ mm, and $t = 0.4$ mm). It is noteworthy that since static analysis is not computationally as expensive as transmissibility, we do not need to consider a minimalistic model, and thus, we retain the 10-layer PnC waveguide during the static analysis step. The highest stress region is encircled in Figs. 9(b), which is 1009 MPa. This value is significantly higher than the allowable stress provided in Equation (7). However, this stress is present in a very localized region, and thus, the structure would try to cope with it by redistributing stress to the rest of the regions after creating localized plastic deformations. On the contrary, the maximum stress in the CS (983 MPa) is distributed through the center of all internal ribs (see Fig. 9(a)). Since the whole member (rib) is affected, this stress is more severe than the former. Thus, the waveguide would likely fail if the cross-sectional stress exceeds the allowable limit. Hence, the design

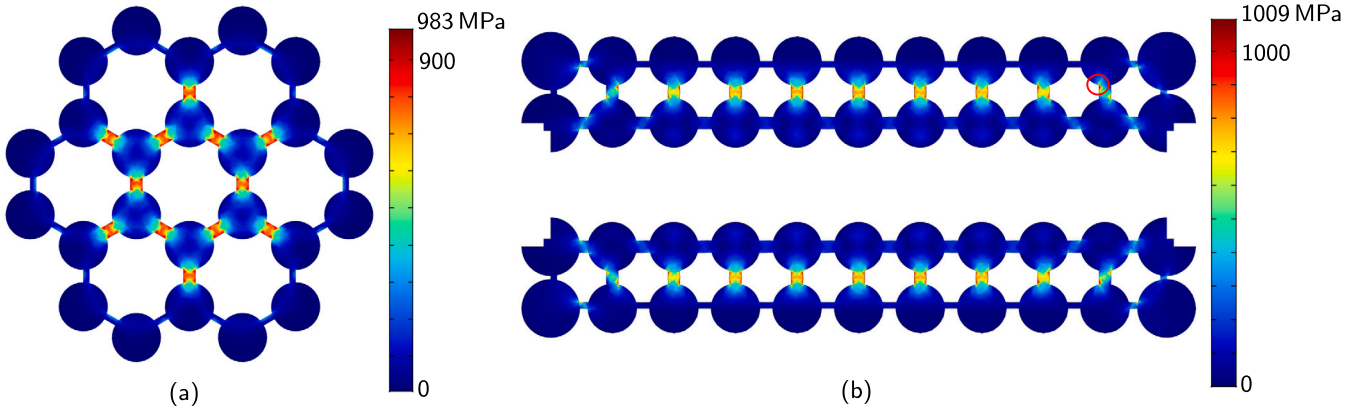

Fig. 9. von Mises stress distributions of the PnC waveguide subjected to a pressure loading, where (a) and (b), respectively, show the cross-sectional (CS) and longitudinal-sectional (LS) views. The maximum stress in LS is a localized value (encircled in (b)), whereas, in CS, it is distributed through internal ribs.

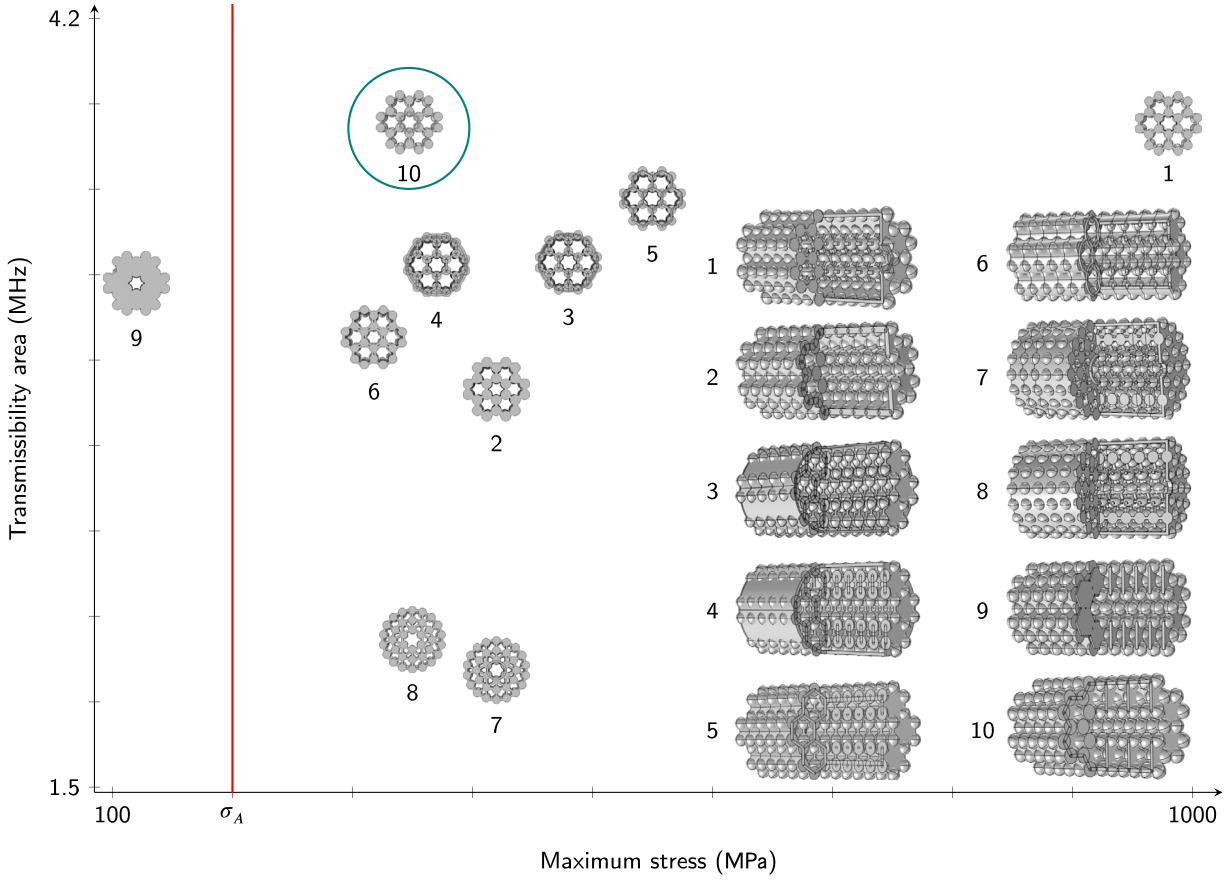

Fig. 10. Transmissibility area vs. maximum von Mises stress for ten different initial designs. The cross-sectional view and 3D view of all designs are also provided in the plot. A desirable design should possess a higher transmissibility area and lower maximum stress. Thus, the design encircled with the ellipse (design 10) is selected, which is a closed hexagonal PnC waveguide with slabs in alternate layers perpendicular to the principal wave propagation direction.

in Fig. 7(c), although it possesses a broad BG, is not a desirable design from the mechanical loading perspective. Thus, we need to expand our design space further to obtain designs that satisfy all the requirements. Therefore, we perform a design space survey by testing various waveguide designs against the two objectives.

3.3.3. *Design space survey: identification of desirable waveguide designs*

We modified the waveguide design to improve the mechanical strength, resulting in ten new designs. They are checked for maximum von Mises stress due to the loading and transmissibility area (TA), which is the area under the transmissibility curve between the required frequency bounds (from 400 kHz to 1.4 MHz, which is the bandwidth of the ultrasound transducer).

Fig. 10 shows different views of these ten designs and compares their performances. The design shown earlier in Fig. 7(c), which was used in both transmissibility and static analyses, is represented as label 1 in the figure. Since the maximum stress is far greater than σ_A, we increase the outer enclosure thickness and the internal rib diameter, resulting in the design labeled 2. These modifications reduced the mechanical stress tremendously (from 983 MPa to 420 MPa). However, it also reduced the TA (from 3.83 MHz to 2.9 MHz); hence, it is not a favorable change. As cylindrical structures are ideal for pressure loads, designs featuring

cylindrical inclusions were investigated. As such, in the designs labeled 3 and 4, the outer shell is replaced with different cylindrical enclosures, thereby decreasing the maximum stress to 480 MPa and 370 MPa, respectively. However, similar to the previous change, the TA also reduced (3.34 MHz for design 3 and 3.33 MHz for design 4); still, design 4 is better than the other three. We also use a different type of cylindrical enclosures where instead of using one cylinder to enclose the waveguide, we add multiple overlapping cylinders to close the waveguide (see designs 5 and 6). Since a circular ring possesses higher strength than a hexagonal ring (a circular ring does not incur bending and has uniform stress for a pressure load), we replaced the straight ribs with curved ribs from design 5, as shown in the design labeled 6. As expected, designs 5 and 6 show superior mechanical performance. We also investigated the influence of combining a cylindrical enclosure and curved beams (see designs 7 and 8). Internal spheres were arranged cylindrically and connected with straight (design 7) and curved (design 8) ribs. Even though both showed improved mechanical strength, their TAs were drastically reduced, leaving them as the least-performing designs. Since all modifications/additions thus far have reduced one objective while improving the other, we need to find parameter(s) whose variations will have a lesser adverse effect on one objective while positively influencing the other. Thus, we introduced cross slabs perpendicular to the primary wave propagation direction. These slabs are subjected to radial loading when the pressure is applied, yielding a considerably lower stress since the radial stiffness is far greater than the bending stiffness. The design labeled 9 possesses slabs in every layer of the waveguide and thus has a maximum stress of 120 MPa, which is almost an order of magnitude lower than design 1 (same design without slabs). However, since all the ribs within the waveguide were replaced, the resulting TA was also reduced excessively. Thus, we propose design 10, where only alternate layers are replaced with slabs; this design possesses almost the same TA as design 1 with a significant reduction in maximum stress (347 MPa compared to 983 MPa of design 1). This exploitation of the design space also provides us with information about the variation in TA across different designs; thus, we choose the minimum required TA as $TA_{req} = 3.5$ MHz. We select design 10 as the preferred geometry, from which the parametric space is further explored.

3.4. Step-4 – Parametric space survey

Using design 10, we further survey the parametric space to obtain designs that show superior performance for all requirements. To that end, we sweep the parameters within their respective ranges (see Table 1). We have updated the ranges for rib diameter ϕ and sphere diameter D after the PUC parametric sweep (see Fig. 6). Additionally, the number of layers in the waveguide n (minimalistic model) was also selected from the transmissibility analysis (see Fig. 8). However, even with this small number of parameters, exploring (and analyzing) each parameter is practically impossible since we have an infinite number of combinations within the design space. Although topology optimization has been used to maximize band gaps in PnCs as discussed in the introduction, the technique is only applicable to the design of a single unit cell [38]. And even for a single unit cell the computational requirements are further reduced by optimizing only on a fraction of the domain in pursuit of symmetric designs—thus enforcing the smallest irreducible Brillouin zone. The excessive computational demands associated with the design of a PnC-based structure composed of a finite number of unit cells preclude the use of topology optimization. In this work we circumvent this difficulty by trimming undesirable regions of the design space by using different criteria, such as the minimum stress constraint, for which a diagonal sweep through the parametric space is used, as discussed next.

3.4.1. Diagonal sweeping

To understand the behavior of the objective functions in a portion of the design space, we vary all design parameters simultaneously (diagonal sweep). To that end, we define a non-dimensional parameter ξ whose ranges are provided in Table 1. As we already know the effects of variations of each parameter on the objectives, we define ξ such that its extreme values satisfy at least one objective. For instance, a small value of ϕ and a large value of D is desirable for maximizing the BG width; however, high values of t and h improve the mechanical strength immensely while reducing the transmissibility. Thus, we ensure that, with an increase in ξ, parameters ϕ, t, and h increase while D decreases.

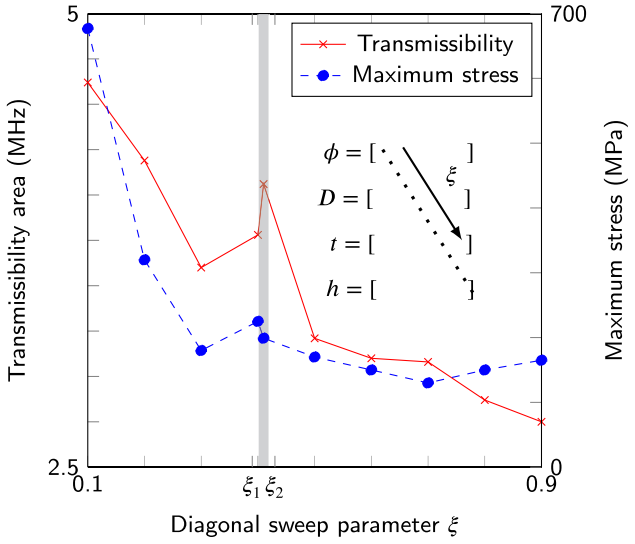

Fig. 11. Variation of transmissibility and maximum stress of the finite waveguide corresponds to a change in the nondimensional parameter ξ. The shaded region shows a sudden response jump due to small variations in ξ ($\xi_1 = 0.4$ to $\xi_2 = 0.41$), indicating that the objective function space is rough in that neighborhood.

Fig. 11 shows both objectives as a function of ξ; notice that the shaded region displays a sudden jump in both objectives. A minute variation in ξ (0.4 to 0.41) results in a considerable change in objectives, implying that the objective functions are highly nonlinear in that vicinity. Additionally, the TA has a steeper jump than the maximum stress. Since the objectives are conflicting, extreme values of ξ only satisfy one objective and thus are removed, resulting in a reduced design space. Additionally, we must select designs with appropriate trade-offs between objectives, which will allow us to trim down the design space further. Thus, instead of a diagonal sweep, we need to sweep through each parameter individually. However, since transmissibility analysis is computationally expensive, we develop surrogate models to reduce the computational cost. The first step is the minimalistic model (6-layer PnC waveguide) discussed in Section 3.3. We further reduce the computational cost of transmissibility analysis by starting with a coarser sample frequency step (e.g., 100 kHz instead of 10 kHz). If the TA of this transmissibility response is much lower than TA_{req}, we trim the design space. After selecting the surrogate model, we proceed to the parametric sweep of the PnC waveguide as described next.

3.4.2. PnC waveguide's parametric sweeping

Parametric sweeping of the waveguide is conducted by sweeping through all the design parameters of the waveguide (ϕ, D, t, and h) similarly to the PUC's parametric sweep discussed in Section 3.2.2. We construct PnC waveguides within this design space and check their performance using static and transmissibility analyses by following the flowchart in Fig. 12. As the static analysis is the least expensive of the two, we first inspect the performance of the waveguide against pressure loading. We further trim the design space if the maximum stress in the PnC waveguide $\sigma_{\max}$ is greater than σ_A. Additionally, if the difference between $\sigma_{\max}$ and σ_A is significantly high, we take larger steps in the parameter space before performing the static analysis again. If

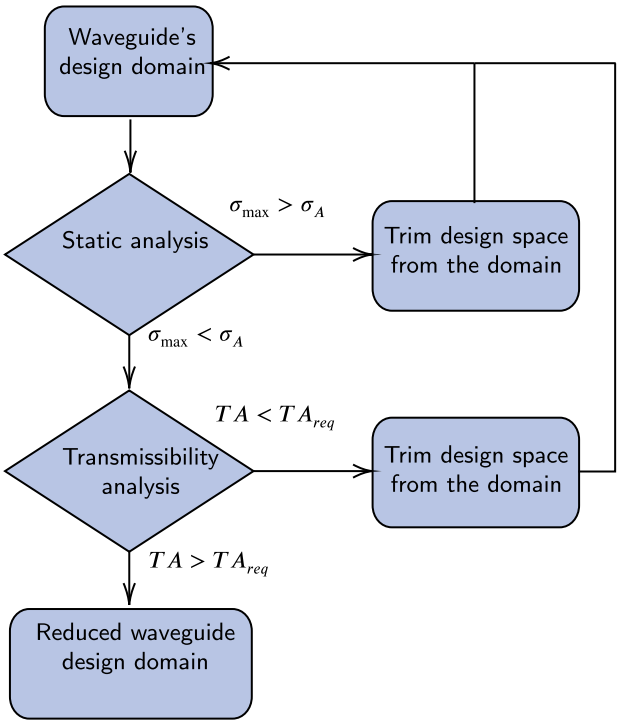

Fig. 12. Flowchart showing the design procedure to trim down the waveguide's design space, including different analyses (static and transmissibility) and corresponding criteria. The order of analysis steps is selected based on their computational cost since, for instance, if a design does not qualify for the static analysis, we do not need to compute expensive transmissibility analysis.

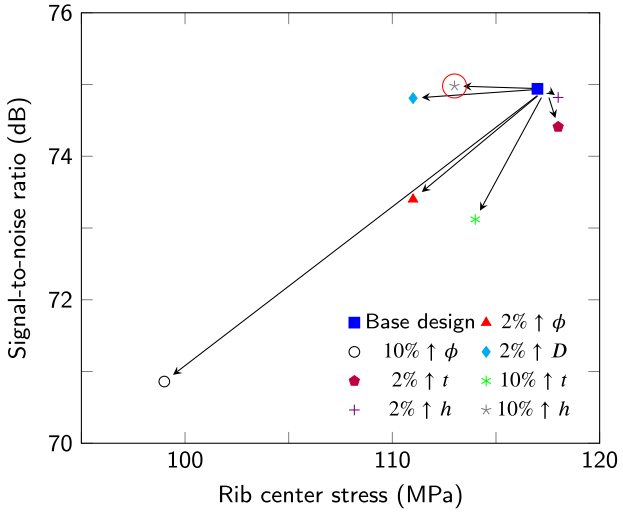

Fig. 13. Sensitivity plot of signal-to-noise ratio and rib center stress corresponding to independent variations of all design parameters, where the desired design is encircled. 2% and 10% variations are used to capture local sensitivities, which are used to further advance the design towards an optimum. Note that we have not provided 10% variation for the sphere diameter D because its value is already close to its upper bound (1.875 mm for the base design) and cannot be increased further.

this sizable parameter step is sufficient to satisfy the static load requirement, we trim the intermediate portion of the design space and proceed to the transmissibility analysis. Otherwise, we choose a subsequent parameter step to create a waveguide design, which is analyzed via static analysis, and the resulting σ_{max} is compared against σ_A. The design that passes through this step is tested using the transmissibility analysis, whereby we compare its TA against TA_{req}, and if TA is much smaller than TA_{req}, we filter the design from the design domain and continue the process similar to the previous step (static analysis). Since both objectives are conflicting, by continuously trimming, we reach a reduced design space possessing designs with adequate trade-offs between both objectives. We see that designs with $\phi < 0.4$ mm, $t < 0.8$ mm, and $h < 0.8$ mm fail to satisfy the static load requirement; similarly, designs with $D < 1.6$ mm and $t > 1.2$ mm have low TA. Thus, the reduced design space is $\phi \subseteq \{0, 4, 0.54\}$, $D \subseteq \{1.6, 1.875\}$, $t \subseteq \{0.8, 1.2\}$, and $h \subseteq \{1, 1.4\}$. We then perform sensitivity analyses to improve the design further, zooming into the design space vicinities and moving towards a Pareto front of optimal designs.

3.5. Sensitivity analysis

Sensitivity analysis determines how an objective function is influenced by the rate of change of the design variable [59]. We use small (2%) and large (10%) variations to generate sensitivities of both objective functions for all the design parameters [60]. Using sensitivities, we zoom into the vicinity of a given design to explore whether further performance improvement is possible. By iteratively performing sensitivity analysis, we move in the direction of the Pareto front, beyond which one can only improve one objective by compromising the performance of the other.

After selecting the lowest bound design ($\phi = 0.4$ mm, $D = 1.6$ mm, $t = 0.8$ mm, and $h = 1$ mm) from the reduced design space, we increment each parameter and calculate objective functions. Noteworthy is that, here, TA has been replaced by the signal-to-noise ratio (SNR) since the former characterizes the PnC waveguide alone; in contrast, the latter incorporates details of the supplied input signal also (see Section 2 and the supplementary material). SNR is obtained by convoluting the PnC waveguide's transmissibility response with the input pulse. The time and frequency responses of the input pulse are provided in the supplementary material. Increasing all parameters except the wall thickness by 10% improved both SNR and rib center stress. After another iteration of a 10% increase in D and h, we arrive at the base design shown in Fig. 13, which is the plot between the two objective functions for different designs and their sensitivities. We repeat the sensitivity analysis until the new sensitivities do not improve the performance of one objective without sacrificing the other. The encircled design from Fig. 13 possesses an SNR of 75 dB with a rib center stress of 113 MPa, which are both desirable objectives. The design marked as a blue diamond could also be an appropriate design; however, its sphere diameter is slightly higher than the upper bound (1.887 mm > 1.875 mm). Similarly, the slab thickness of the encircled design is also close to its upper limit; thus, further zooming in the vicinity of these two designs is difficult. Hence, the encircled design is selected as the desired final design with parameters: $\phi = 0.44$ mm, $D = 1.85$ mm, $t = 0.8$ mm, and $h = 1.4$ mm.

3.6. Inspection of the PnC waveguide fabricated via additive manufacturing

The final design's parameters are still difficult to realize using SS316 via available 3D printing technology (selective laser sintering) due to the high decimal precision (0.01 mm) used in the design process. Due to the intricacy of the design—i.e., multiple orientations of the ribs, large flat surfaces that are normal to the printing orientation, and the outer enclosure—currently available additive manufacturing technology cannot achieve the desired manufacturing tolerances. Thus, we fabricate a 3D PnC waveguide with slightly different design parameters, i.e., $\phi = 0.5$ mm, $D = 1.8$ mm, $t = 1$ mm, and $h = 1$ mm, whose photograph is shown in Fig. 14(a). Noteworthy, these modifications will affect the waveguide's performance; however, they are not so significant since the waveguide still satisfies all design requirements. To compare the feature size and shape with the design, we performed a computer tomography (CT) scan of the specimen using a micro-CT scanner (Phoenix Nanotom). The rib diameter, sphere diameter, and wall thickness are consistent between the design and the printed part, with slight varia-

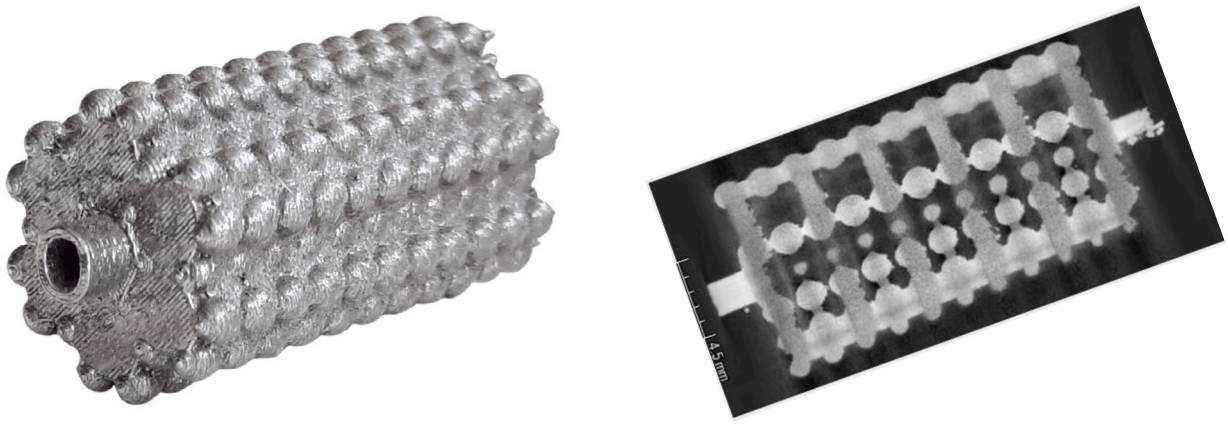

(a) (b)

Fig. 14. (a) The photograph of a 3D PnC waveguide realized via metal additive manufacturing (selective laser sintering). (b) The CT scan of the longitudinal section through the center of the fabricated PnC waveguide shows the internal features. The difference in the feature sizes along the length is due to the orientation of the specimen in the micro-CT scanner, which distorted its view.

tions. However, the slab thickness experienced a 15 % average increase during manufacturing. The cross-sectional and longitudinal-sectional views of the PnC waveguide's CT scan with parameter measurements are provided in the supplementary material. The increase in the slab thickness could further improve the mechanical resistance. In addition, the outer surface of the waveguide is rough, as shown in Figs. 14(a) and 14(b), which could influence its transmission behavior. Since a rough surface always creates more resistance to wave propagation than a smooth one, the increased surface roughness could be an advantage in reducing wave transmission. However, since we deal mainly with bulk rather than surface waves, this influence would also be minimal in the performance of the PnC waveguide.

4. Summary and conclusions

In this paper, we presented a methodology for the design of a phononic crystal waveguide that maximizes wave attenuation while minimizing mechanical stress. We incorporated additional aspects to the design process, such as manufacturing considerations, domain size limitations, and industrial standards. Since various computationally expensive analyses were required, we used surrogate models, thereby minimizing analysis costs. By means of a parametric sweep we could explore the multi-dimensional design space in pursuit of an adequate design. Additionally, using sensitivity analysis, we obtained an adequate design that is part of a Pareto front, which satisfies all constraints. We realized that design via additive manufacturing and inspected using a micro-CT scanner.

Our concluding remarks are:

- For a single-phase 3D solid PnC, although the BG width increases with the contrast between the adjacent members' dimensions within the PUC, a maximum value exists beyond which any increase in dimensions decreases the BG width. This behavior is because, beyond the optimum value, any attempt to increase the contrast in properties (mass and/or stiffness) by changing the dimensions of the PUC's internal features results in a decrease in the mechanical impedance mismatch, thereby lowering the BG width;
- When attempting to maximize the performance of PnCs (or similar structures) to conflicting objectives, it is necessary to identify parameters whose variations do not influence the objectives adversely. In our case, we selected the thickness of slabs in alternate layers. Increasing this thickness improves mechanical strength tremendously while having little influence on wave attenuation behavior;
- While solving a multi-objective design problem within a design space consisting of several parameters (five in our case), it is necessary to trim the design space if associated analyses are computationally expensive. The trimming criteria can be derived from the design requirements and the objective functions' response to the parameters;

As a further step, we can generalize this design procedure to apply to other multi-objective problems having expensive and/or contradicting objectives with appropriate modifications in selecting the design parameters, analysis steps, and design space trimming criteria.

CRediT authorship contribution statement

Sabiju Valiya Valappil: Writing – original draft, Methodology, Investigation, Formal analysis, Conceptualization. **Johannes F.L. Goosen:** Writing – review & editing, Supervision, Conceptualization. **Alejandro M. Aragón:** Writing – review & editing, Supervision, Methodology, Conceptualization.

Declaration of competing interest

The authors declare the following financial interests/personal relationships which may be considered as potential competing interests:

Alejandro M. Aragon has patent #UltrasonicTransducerandUltrasonicFlowmeter (US2023/0130690) issued to A.M. Aragon, S.V. Valappil, and J. Hogendoorn.

Data availability

Data will be made available on request.

Acknowledgements

We gratefully appreciate the support from the Topconsortia voor Kennis en Innovatie (TKI) project grant and our sponsoring partner, Krohne.

Appendix A. Supplementary material

Supplementary material related to this article can be found online at https://doi.org/10.1016/j.matdes.2023.112594.

References

[1] Mahmoud Meribout, Abdelwahid Azzi, Nabil Ghendour, Nabil Kharoua, Lyes Khezzar, Esra AlHosani, Multiphase flow meters targeting oil & gas industries, Measurement 165 (2020) 108111.

[2] Yong Chen, Yiyong Huang, Xiaoqian Chen, Acoustic propagation in viscous fluid with uniform flow and a novel design methodology for ultrasonic flow meter, Ultrasonics 53 (2) (2013) 595–606.

[3] M. Kupnik, A. Schroder, P. O'Leary, E. Benes, M. Groschl, Adaptive pulse repetition frequency technique for an ultrasonic transit-time gas flowmeter for hot pulsating gases, IEEE Sens. J. 6 (4) (2006) 906–915.

[4] H.-H. Eckstein, M. Eichbaum, K. Klemm, A. Doerfler, P. Ringleb, T. Bruckner, J.-R. Allenberg, Improvement of carotid blood flow after carotid endarterectomy—evaluation using intraoperative ultrasound flow measurement, Eur. J. Vasc. Endovasc. Surg. 25 (2) (2003) 168–174.

[5] Richard Smith, Douglas R. Sparks, Diane Riley, Nader Najafi, A mems-based Coriolis mass flow sensor for industrial applications, IEEE Trans. Ind. Electron. 56 (4) (2009) 1066–1071.

[6] Jankees Hogendoorn, Karsten Tawackolian, Peter van Brakel, Jeroen van Klooster, Jan Drenthen, High viscosity hydrocarbon flow measurement: a challenge for ultrasonic flow meters?, in: 27th International North Sea Flow Measurement Workshop, 2009.

[7] Pierre Ueberschlag, Andreas Berger, Michal Bezdek, Ultrasonic transducer for application in an ultrasonic, flow measuring device or in an ultrasonic, fill-level measuring device, US Patent 10,620,026, April 14, 2020.

[8] Emanuel J. Gottlieb, Kevin P. Minnock, Donald R. Augenstein, Richard A. Zuckerman, Acoustically isolated ultrasonic transducer housing and flow meter, US Patent 9,506,789, November 29, 2016.

[9] Jeroen Martin Van Klooster, Flowmeter, US Patent 6,799,475, October 5, 2004.

[10] A. Ramos, J.L. San Emeterio, P.T. Sanz, Improvement in transient piezoelectric responses of nde transceivers using selective damping and tuning networks, IEEE Trans. Ultrason. Ferroelectr. Freq. Control 47 (4) (2000) 826–835.

[11] M.S. Kushwaha, P. Halevi, L. Dobrzynski, B. Djafari-Rouhani, Acoustic band structure of periodic elastic composites, Phys. Rev. Lett. 71 (Sep. 1993) 2022–2025.

[12] W.L. Bragg, The diffraction of short electromagnetic waves by a crystal, Scientia 23 (45) (1929) 153.

[13] Caiyou Zhao, Junyuan Zheng, Tao Sang, Liuchong Wang, Qiang Yi, Ping Wang, Computational analysis of phononic crystal vibration isolators via fem coupled with the acoustic black hole effect to attenuate railway-induced vibration, Constr. Build. Mater. 283 (2021) 122802.

[14] K. Petrover, A. Baz, Finite element modeling of one-dimensional nonreciprocal acoustic metamaterial with anti-parallel diodes, J. Acoust. Soc. Am. 148 (1) (Jul. 2020) 334–346.

[15] Kyung Hoon Lee, Hasan Al Ba'ba'a, Kunhao Yu, Ketian Li, Yanchu Zhang, Haixu Du, Sami F. Masri, Qiming Wang, Magnetoactive acoustic topological transistors, Adv. Sci. 9 (18) (2022) 2201204.

[16] Guobiao Hu, Lihua Tang, Junrui Liang, Chunbo Lan, Raj Das, Acoustic-elastic metamaterials and phononic crystals for energy harvesting: a review, Smart Mater. Struct. 30 (8) (Jul. 2021) 085025.

[17] Hrishikesh Danawe, Gorkem Okudan, Didem Ozevin, Serife Tol, Conformal gradient-index phononic crystal lens for ultrasonic wave focusing in pipe-like structures, Appl. Phys. Lett. 117 (2) (Jul. 2020) 021906.

[18] Fuyin Ma, Zhen Huang, Chongrui Liu, Jiu Hui Wu, Acoustic focusing and imaging via phononic crystal and acoustic metamaterials, J. Appl. Phys. 131 (1) (Jan. 2022) 011103.

[19] Craig W. Broadman, Christina J. Naify, Michael J. Lee, Michael R. Haberman, Design of a one-dimensional underwater acoustic leaky wave antenna using an elastic metamaterial waveguide, J. Appl. Phys. 129 (19) (May 2021) 194902.

[20] Changqing Xu, Ze-Guo Chen, Guanqing Zhang, Guancong Ma, Ying Wu, Multi-dimensional wave steering with higher-order topological phononic crystal, Sci. Bull. 66 (17) (2021) 1740–1745.

[21] Mahdiyeh Ghoreshi, Ali Bahrami, Acoustic invisibility cloak based on two-dimensional solid-fluid phononic crystals, Solid State Commun. 342 (2022) 114646.

[22] Peng Chen, Michael R. Haberman, Omar Ghattas, Optimal design of acoustic metamaterial cloaks under uncertainty, J. Comput. Phys. 431 (2021) 110114.

[23] Mohamed Farhat, Sebastien Guenneau, Stefan Enoch, Ultrabroadband elastic cloaking in thin plates, Phys. Rev. Lett. 103 (2) (2009) 024301.

[24] Wen Kang Cao, Cheng Zhang, Wu Li Ting, Kai Qi Guo, Jun Chen Ke, Tie Jun Cui, Qiang Cheng, Tunable acoustic metasurface for three-dimensional wave manipulations, Phys. Rev. Appl. 15 (Feb. 2021) 024026.

[25] A-Li Chen, Yue-Sheng Wang, Yan-Feng Wang, Hong-Tao Zhou, Si-Min Yuan, Design of acoustic/elastic phase gradient metasurfaces: principles, functional elements, tunability, and coding, Appl. Mech. Rev. 74 (2) (Jun. 2022) 020801.

[26] Kai Wu, Jing-Jing Liu, Yu-jiang Ding, Wei Wang, Bin Liang, Jian-Chun Cheng, Metamaterial-based real-time communication with high information density by multipath twisting of acoustic wave, Nat. Commun. 13 (1) (Sep. 2022) 5171.

[27] Tinggui Chen, Wenting Li, Dejie Yu, A tunable gradient acoustic metamaterial for acoustic sensing, Extrem. Mech. Lett. 49 (2021) 101481.

[28] Fabrice Lemoult, Mathias Fink, Geoffroy Lerosey, Acoustic resonators for far-field control of sound on a subwavelength scale, Phys. Rev. Lett. 107 (Aug. 2011) 064301.

[29] Karl F. Graff, Wave Motion in Elastic Solids, Courier Corporation, 2012.

[30] Walter Benenson, John W. Harris, Horst Stocker, Holger Lutz, Handbook of Physics, Springer, 2002.

[31] István L. Vér, Leo L. Beranek, Noise and Vibration Control Engineering: Principles and Applications, John Wiley & Sons, 2005.

[32] X.K. Han, Z. Zhang, Bandgap design of three-phase phononic crystal by topological optimization, Wave Motion 93 (2020) 102496.

[33] Atul Kumar Sharma, Majd Kosta, Gal Shmuel, Oded Amir, Gradient-based topology optimization of soft dielectrics as tunable phononic crystals, Compos. Struct. 280 (2022) 114846.

[34] Qiangbo Wu, Jingjie He, Wenjiong Chen, Quhao Li, Shutian Liu, Topology optimization of phononic crystal with prescribed band gaps, Comput. Methods Appl. Mech. Eng. 412 (2023) 116071.

[35] Xiaopeng Zhang, Yan Li, Yaguang Wang, Zhiyuan Jia, Yangjun Luo, Narrow-band filter design of phononic crystals with periodic point defects via topology optimization, Int. J. Mech. Sci. 212 (2021) 106829.

[36] Anna Dalklint, Mathias Wallin, Katia Bertoldi, Daniel Tortorelli, Tunable phononic bandgap materials designed via topology optimization, J. Mech. Phys. Solids 163 (2022) 104849.

[37] Xing Zhang, Hongling Ye, Nan Wei, Ran Tao, Zhen Luo, Design optimization of multifunctional metamaterials with tunable thermal expansion and phononic bandgap, Mater. Des. 209 (2021) 109990.

[38] Sanne J. van den Boom, Reza Abedi, Fred van Keulen, Alejandro M. Aragón, A level set-based interface-enriched topology optimization for the design of phononic crystals with smooth boundaries, Comput. Methods Appl. Mech. Eng. 408 (2023) 115888.

[39] Ole Sigmund, Jakob Søndergaard Jensen, Systematic design of phononic band–gap materials and structures by topology optimization, Philos. Trans. R. Soc. Lond. A, Math. Phys. Eng. Sci. 361 (1806) (2003) 1001–1019.

[40] Maximilian Wormser, Fabian Wein, Michael Stingl, Carolin Körner, Design and additive manufacturing of 3d phononic band gap structures based on gradient based optimization, Materials 10 (2017).

[41] Weibai Li, Fei Meng, Yang fan Li, Xiaodong Huang, Topological design of 3d phononic crystals for ultra-wide omnidirectional bandgaps, Struct. Multidiscip. Optim. 60 (6) (2019) 2405–2415.

[42] Claudio Quaglia, Elisa Buselli, Robert J. Webster, Pietro Valdastri, Arianna Menciassi, Paolo Dario, An endoscopic capsule robot: a meso-scale engineering case study, J. Micromech. Microeng. 19 (10) (Sep. 2009) 105007.

[43] Sabiju Valiya Valappil, Johannes F.L. Goosen, Alejandro M. Aragón, Phononic crystals for suppressing crosstalk in ultrasonic flowmeters, IEEE Trans. Instrum. Meas. 72 (2023) 1–11.

[44] Joseph L. Rose, A baseline and vision of ultrasonic guided wave inspection potential, J. Press. Vessel Technol. 124 (3) (Jul. 2002) 273–282.

[45] J. Yin, S. Zhang, H.W. Zhang, B.S. Chen, Band structure and transmission characteristics of complex phononic crystals by multi-level substructure scheme, Int. J. Mod. Phys. B 29 (04) (2015) 1550013.

[46] Q. Aumann, M. Miksch, G. Müller, Parametric model order reduction for acoustic metamaterials based on local thickness variations, J. Phys. Conf. Ser. 1264 (Jul. 2019) 012014.

[47] Zian Jia, Yanyu Chen, Haoxiang Yang, Lifeng Wang, Designing phononic crystals with wide and robust band gaps, Phys. Rev. Appl. 9 (Apr. 2018) 044021.

[48] Ahmed Mehaney, Hussein A. Elsayed, Hydrostatic pressure effects on a one-dimensional defective phononic crystal comprising a polymer material, Solid State Commun. 322 (2020) 114054.

[49] William E. Frazier, Metal additive manufacturing: a review, J. Mater. Eng. Perform. 23 (6) (2014) 1917–1928.

[50] Y.S. Liao, J.T. Huang, Y.H. Chen, A study to achieve a fine surface finish in wire-edm, in: 14th International Symposium on Electromachining (ISEM XIV), J. Mater. Process. Technol. 149 (1) (2004) 165–171.

[51] Charles Kittel, Paul McEuen, Kittel's Introduction to Solid State Physics, John Wiley & Sons, 2018.

[52] Felix Bloch, Quantum mechanics of electrons in crystal lattices, Z. Phys. 52 (1928) 555–600.

[53] A. Bedford, D.S. Drumheller, Elastic Wave Propagation, John Wileg & Sons, 1994, pp. 151–165.

[54] L. D'Alessandro, E. Belloni, R. Ardito, A. Corigliano, F. Braghin, Modeling and experimental verification of an ultra-wide bandgap in 3d phononic crystal, Appl. Phys. Lett. 109 (22) (2016) 221907.

[55] Thomas J.R. Hughes, The Finite Element Method: Linear Static and Dynamic Finite Element Analysis, Courier Corporation, 2012.

[56] J.E. Shigley, C.R. Mischke, R.G. Budynas, Mechanical Engineering Design, 7th ed., McGraw-Hill, 2004.

[57] Mingming Ma, Zemin Wang, Dengzhi Wang, Xiaoyan Zeng, Control of shape and performance for direct laser fabrication of precision large-scale metal parts with 316l stainless steel, Opt. Laser Technol. 45 (2013) 209–216.

[58] Ductile iron pipes, fittings, accessories and their joints for water applications. Standard, International Organization for Standardization, Geneva, CH, December 2009.

[59] Saman Razavi, Hoshin V. Gupta, What do we mean by sensitivity analysis? The need for comprehensive characterization of "global" sensitivity in Earth and environmental systems models, Water Resour. Res. 51 (5) (2015) 3070–3092.

[60] Jérôme Morio, Global and local sensitivity analysis methods for a physical system, Eur. J. Phys. 32 (6) (Oct. 2011) 1577–1583.